



OH radical measurements in combustion environments using wavelength modulation spectroscopy and dual-frequency comb spectroscopy near 1491 nm

Torrey R. S. Hayden¹ · Nathan Malarich¹ · Dan Petrykowski¹ · Siddharth P. Nigam¹ · Jason D. Christopher¹ · Caelan Lapointe¹ · Nicholas T. Wimer¹ · Peter E. Hamlington¹ · Gregory B. Rieker¹

Received: 7 February 2019 / Accepted: 30 October 2019 / Published online: 9 November 2019
© Springer-Verlag GmbH Germany, part of Springer Nature 2019

Abstract

Hydroxyl radical (OH) is a key intermediate reactive species during combustion processes relevant to power production, transportation, and manufacturing. We demonstrate an OH sensor based on in situ laser absorption spectroscopy for deployment in industrial conditions. The sensor relies on telecommunications-fiber-coupled, tunable-diode-laser absorption spectroscopy of an OH transition near 1491 nm. By employing wavelength modulation spectroscopy, the sensor is capable of in situ, quantitative detection of OH down to mole fraction values of 10^{-5} over a 75-cm pathlength. To increase the accuracy of the OH sensor, we perform the first dual-comb spectroscopy measurement above a flame and use the results to create an absorption database of water vapor transitions from 1489.2 to 1492.5 nm at temperatures up to 2165 K. The database is included in the analysis procedure for the tunable diode laser sensor to account for the water vapor absorption that overlaps with the OH absorption. The utility of the laser sensor is demonstrated by characterizing the concentration of OH radical above a catalytic combustor under different operating conditions.

1 Introduction

Hydroxyl radical (OH) is of diagnostic interest because of its key role in combustion kinetics and surface modification manufacturing processes. In combustion, it is a prevalent intermediate that can map the flame structure and indicate combustion completeness. In manufacturing, OH stimulates surface treatment of polypropylene [1, 2] and also appears in dielectric discharge plasmas used for material and gas stream processing [3–6]. Thus, diagnostics that provide temporal and spatial measurements of OH can aid in optimizing the operation of industrial flame systems. However, OH is difficult to measure in industrial settings because extractive samples from techniques such as gas chromatography are not representative of flame conditions (OH is highly reactive

and temperature sensitive), and in situ measurements are complicated by high temperatures, limited optical access, and generally harsh deployment conditions.

Laser-induced fluorescence (LIF) and planar laser-induced fluorescence (PLIF) are the most widespread approaches to measuring OH and have been used with great success to image OH concentrations in many combustion applications [7–15]. These methods have provided measurements of small quantities of OH radical in a variety of combustion settings; however, they require some combination of high-power laser equipment, significant optical access, and/or sensitive optical sub-systems that are challenging for industrial application and real-time monitoring.

Laser absorption spectroscopy is a preferred option for probing many industrial combustion and plasma systems because it is quantitative, relatively simple, can probe large systems, and requires only one or two small optical ports. In laser absorption spectroscopy, the thermodynamic properties (temperature, pressure, etc.) and concentration of a species of interest can be measured by their relationship to the absorption of laser light with a photon energy matching the energy of a quantum mechanical transition of the target species. Various research groups have used absorption spectroscopy to probe the electronic transitions of OH

Electronic supplementary material The online version of this article (<https://doi.org/10.1007/s00340-019-7341-6>) contains supplementary material, which is available to authorized users.

✉ Torrey R. S. Hayden
torrey.hayden@colorado.edu

¹ Mechanical Engineering Department, University of Colorado at Boulder, UCB 427, Boulder, CO, USA

in the ultraviolet–visible (UV–Vis) wavelength range for a variety of applications including shock-tubes, engines, and the atmosphere [4, 16–20]. Although the electronic transitions of OH in the UV–Vis range are very strong, it can also be desirable to probe weaker ro-vibrational transitions at near-infrared (NIR) wavelengths. NIR sensors are desirable because of the low-cost and fiber-coupled nature of the available lasers. Despite these advantages, there has been limited work on OH absorption spectroscopy in this region. Both Peeters et al. [21] and Rutkowski et al. [22] used cavity-enhanced absorption techniques near 1500 nm to detect OH concentrations in flame environments. For large, long-term industrial deployment, it is desirable to pursue open-path, non-cavity enhanced approaches such as direct absorption or wavelength modulation spectroscopy with tunable diode lasers.

Wavelength modulation spectroscopy (WMS) is a form of absorption spectroscopy that achieves higher sensitivity than traditional direct absorption spectroscopy by reducing the effects of system noise and intensity fluctuations. Aizawa [23, 24] previously demonstrated the use of WMS to detect OH radical near 1550 nm. These papers highlight the challenges of making accurate OH measurements, namely low OH absorption signal levels and interference from high-temperature H₂O absorption.

It is not possible to find OH transitions in the infrared spectral regions that are free from significant (10–80%) interference from nearby H₂O transitions. The overlap between the absorption of OH and H₂O in the 1490–1492 nm region is shown in the simulated absorbance in Fig. 1. This overlap is significant because a WMS measurement detects the combined absorption of any overlapping species. In order to calculate OH mole fraction from the measured WMS signal, a model of the underlying H₂O absorption must be included in the fit of the measured signal to account for the added signal. Although spectral databases such as HITRAN or HITEMP contain absorption transition information for H₂O near 1491 nm, the high-temperature H₂O parameters in this wavelength region are extrapolated from ambient conditions and have never been experimentally investigated or validated [25, 26]. It has been shown by several past researchers that these databases are increasingly uncertain as temperatures approach combustion conditions [27–29]. Hence, careful characterization of the H₂O transitions neighboring the strong OH transitions of interest in the 1491-nm range are required in order to develop an accurate OH sensor.

Here, we improve the accuracy of an OH sensor operating near 1491 nm by developing an updated high-temperature water vapor absorption database in this region using dual-frequency comb spectroscopy and multispectral fitting. A premixed ribbon burner system is used as the stable high-temperature environment in which to measure

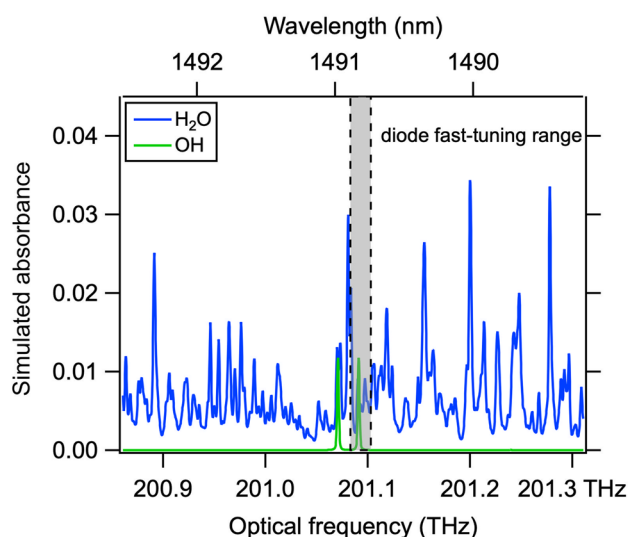


Fig. 1 Simulated absorbance of 15% H₂O and 0.3% OH mole fraction from 200.9 to 201.4 THz (1489–1493 nm) using HITEMP 2010 for OH and the spectral linelist developed in this paper for H₂O. Both species were simulated at 2200 K, 820 mbar, and a pathlength of 30.7 cm. Shaded region indicates the tuning range of DFB diode laser used for WMS measurements. The range of the dual-frequency comb spectrometer extends beyond the plot from 196.2 to 217.2 THz (1380–1528 nm)

these spectral parameters. The light from a dual-frequency comb spectrometer is passed through the ribbon burner system operating at several different equivalence ratios in order to measure absorption parameters at different thermodynamic conditions. We then extract linestrength and linecenter for the strongest transitions using the multispectral fitting code described in [30, 31]. The dual-frequency comb spectrometer can measure all of the H₂O and OH transitions simultaneously with broad bandwidth, high resolution, and a well-known wavelength axis to minimize the uncertainty of the extracted spectral parameters [29]. These are the first dual-comb spectroscopy measurements in a flame environment.

Finally, we build on the work of Aizawa et al. by incorporating the H₂O absorption database into a WMS-based sensor for measuring OH at 1491 nm. We utilize $1f$ normalization of the $2f$ signal to mitigate beam steering in the WMS sensor and use an improved WMS fitting routine to reduce uncertainties in extracted thermodynamic values. We demonstrate the sensor by probing the product gases above the surface of a catalytic combustor (which is nominally expected to be a radical-free heat source) for OH presence at different combustion conditions. This demonstration shows the benefit of the WMS OH sensor, which in this case is able to characterize conditions under which the combustor produces OH radical above the surface.

2 Measurement approaches

2.1 Absorption spectroscopy

Wavelength modulation spectroscopy and dual-frequency comb spectroscopy are both forms of absorption spectroscopy. Absorption spectroscopy is the quantification of the light absorbed by a gas sample as a function of the incident wavelength. The light is absorbed if the wavelength matches the energy of a quantum transition between energy states in an atom or molecule. The amount of light absorbed, which is quantified as absorbance, α_λ , is directly related to the bulk thermodynamic properties of the probed gas sample through Beer's law, Eq (1):

$$\alpha_\lambda = -\ln\left(\frac{I_t}{I_0}\right)_\lambda = S(T)P\chi L\phi_\lambda \quad (1)$$

where I_t is the transmitted intensity of the light after it has passed through the sample, I_0 is the initial (un-attenuated) intensity, and λ is the wavelength of the laser light that passes through the gas sample.

As shown in Eq. (1), the absorbance can be represented by the product of the linestrength of the absorbing transition at a given temperature $S(T)$, the total pressure P , the species mole fraction of the absorbing gas X_{abs} , the pathlength of the laser across the gas L , and the absorption lineshape ϕ_λ . Thus, the absorbance is explicitly related to the thermodynamic properties T , X , P , and implicitly related to the quantum properties of the target gas through the linestrength and lineshape terms.

In many atmospheric-pressure systems, it is sufficient to model the lineshape as a Voigt profile—a convolution of the Gaussian and Lorentz profiles that captures the collisional and Doppler broadening of the absorption transition. The four components of the Voigt profile are the center wavelength, integrated area, Lorentz width, and Doppler width. The Doppler width is not transition-specific and is calculated only from the wavelength of the transition and the temperature of the gas. The other quantities are transition-specific and are calculated from linecenter, pressure-shift coefficient, linestrength, foreign and self-broadening coefficients, and their temperature dependence, which are all catalogued in spectral databases such as HITRAN and HITEMP or measured line lists [25, 26, 28, 29].

2.2 Scanned wavelength modulation spectroscopy (WMS) for industrial OH sensing

For the industrial OH sensor, we use $1f$ -normalized WMS, which is a sensitive form of absorption spectroscopy. WMS is an excellent choice for industrial applications because of its kilohertz time resolution, compact size, relatively low

cost, and compatibility with telecom fiber optic cables of the semiconductor diode lasers [32–46]. In WMS, the wavelength and intensity of the laser are modulated at a fast frequency, f , (typically 10–100's of kHz), which results in a series of harmonics in the detector signal. The harmonics in the detector signal can be isolated using a lock-in amplifier, which acts as a bandpass filter centered at the frequency of interest. We are particularly interested in the second harmonic signal, $2f$, because its magnitude is related to the absorbance and can be used to extract thermodynamic properties. Normalization of the $2f$ by the first harmonic, $2f/1f$, enables absolute measurements and removes the effects of intensity fluctuations due to beam steering, window fouling, and vibrating optics [36].

The experimental equipment used for WMS measurements is shown in the top-right box in Fig. 2. Laser current and temperature are controlled by an ILX laser diode controller. Two National Instruments PCI-6110 data acquisition boards supply the modulation voltage to the ILX laser diode controller and acquire the output voltages from the photodetectors. Light from the three lasers is combined and passed to two fibers, one that sends the light to the gas sample via a transmit collimator and another that passes the light directly to a photodetector for intensity monitoring or alternatively to a fiber-based etalon (FSR = 636 MHz) to characterize the wavelength modulation.

By fitting the WMS signal to obtain the integrated absorbance according to the procedures in [47], we eliminate the dependence on the lineshape, ϕ_λ , as the integral of ϕ_λ is unity by definition. The result is shown in Eq. (2) below:

$$A = \int \alpha d\lambda = S(T)PX_{\text{abs}}L \quad (2)$$

The integrated area is thus only a function of the linestrength, pressure, absorbing-species mole fraction, and pathlength. Temperature can be calculated using the ratio, A_1/A_2 , from two transitions of the same species [48], removing the dependence of the temperature measurement on pressure and mole fraction. Absorbing-species mole fraction can then be calculated by solving Eq. (2) for X_{abs} , with measured pressure, pathlength, and temperature.

As discussed in the previous section and shown in Fig. 1, an absorption measurement of OH at 1491 nm will also include overlapping H₂O absorption. Therefore, analysis of OH must remove the H₂O absorption contribution in order to isolate the OH integrated absorbance. Therefore, we measure the temperature and H₂O mole fraction using two diode lasers which probe two interference-free H₂O transitions at 1392 nm and 1469 nm [47]. The integrated areas extracted from these two transitions are used to calculate temperature and H₂O mole fraction following the technique described above. A third diode laser probes

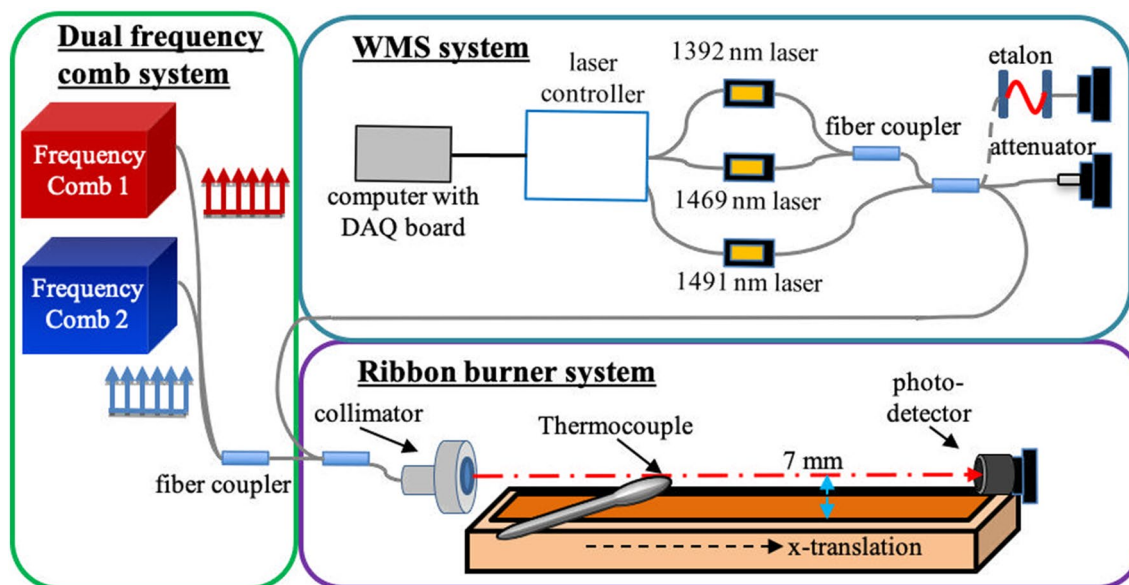


Fig. 2 Schematic of the optical setup used for all ribbon burner experiments. (left) Light from two frequency combs is combined to pass across the flame 7 mm above the edge of the burner for extraction of high-temperature spectral parameters. (top-right) Experiment-

tal setup for WMS OH sensor in the premixed flame of the ribbon burner. (bottom-right) A thermocouple is mounted on a translation stage coincident with the laser beam in the flame to test for flame uniformity

the OH transition near 1491 nm. We use the measured temperature and H_2O mole fraction to simulate H_2O absorbance as a function of wavelength in the 1491-nm region and incorporate this simulated absorbance into the fit of the OH transition. Specifically, the fit treats the OH transition as a floating Voigt lineshape added to the H_2O absorbance. The summed absorbance of H_2O and OH is then incorporated into Eq. (1) with the measured intensity and wavelength variations of the diode laser to simulate the transmitted intensity, I_t . The simulated transmitted intensity passes through the lock-in amplifier to isolate the $2f/1f$ signal, shown in Fig. 3. The simulated $2f/1f$ signal is then fit to the measured data by varying the parameters of the Voigt lineshape of the single OH transition until residuals between the model and the measured WMS signal are minimized. An example of a measured $2f/1f$ signal and the corresponding model fit using the database derived here in this paper is shown at the bottom of Fig. 3. The integrated absorbance for the single OH transition that minimizes residuals is used to calculate OH mole fraction.

The absolute accuracy of the OH measurement is highly dependent on the quality of the underlying H_2O database used to simulate H_2O absorbance as a function of wavelength in the analysis. There have been no known database measurements of H_2O in this 1490–1493 nm region, which means that the best available data are from HITEMP 2010. The line parameters of HITEMP in this region have 10–20% uncertainty as they are calculated from quantum models. This uncertainty correlates to significant uncertainty in

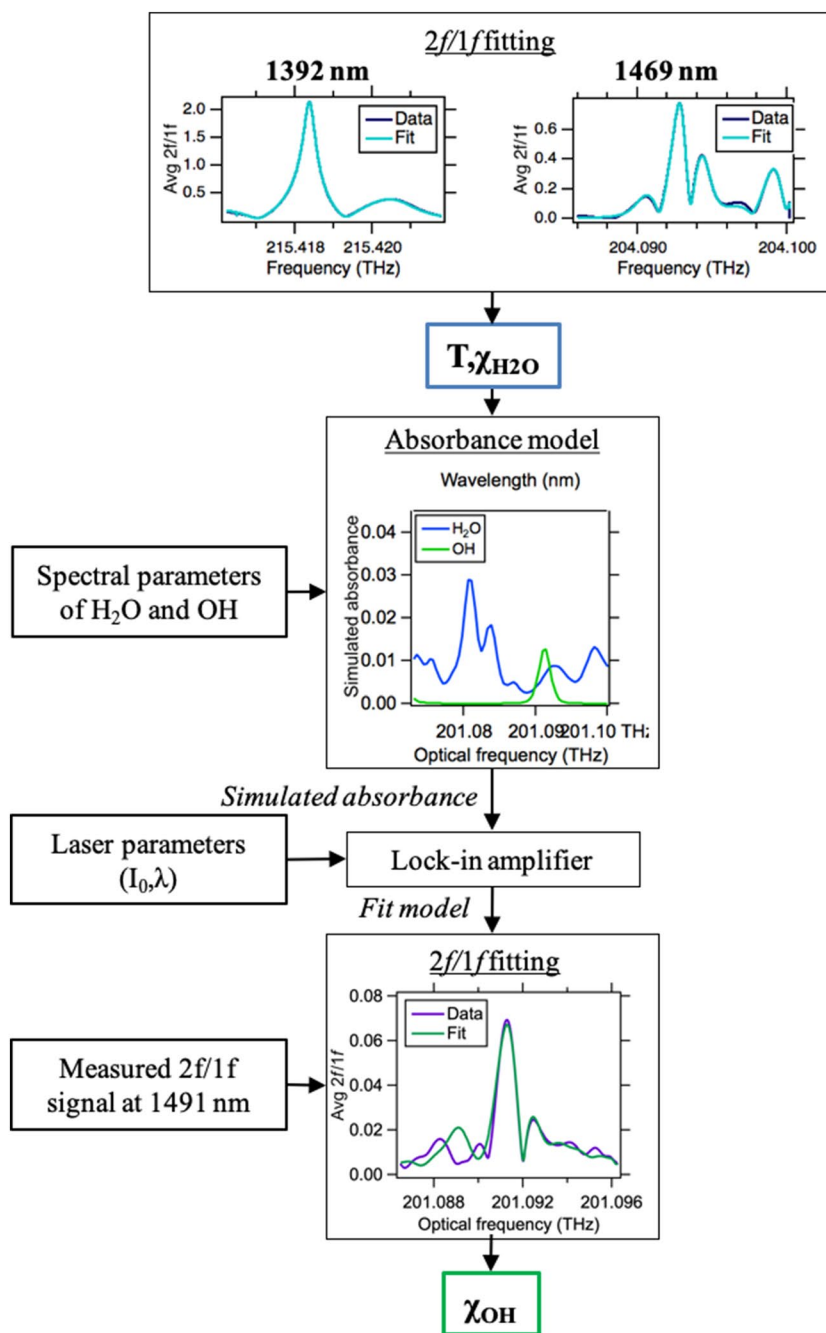
the OH measurement. Hence, we measure the spectral line parameters of the H_2O transitions in this region using dual-frequency comb spectroscopy to improve the accuracy of our OH measurement.

2.3 Dual-frequency comb spectroscopy (DCS) for H_2O database development

Dual-frequency comb spectrometers are an emerging class of laser spectrometers that provide simultaneously broad spectral bandwidth, high spectral resolution, and excellent wavelength accuracy [49]. With these characteristics, the dual-frequency comb spectrometer is well-suited for the development of spectral databases, particularly for high-temperature environments [28, 29, 50, 51]. Dual-frequency comb spectrometers are recently also capable of field deployment to industrial environments [52, 53], but currently at a higher cost and slower measurement rate than tunable diode laser systems. Thus, we use frequency comb spectroscopy here to develop the high-temperature database for interfering water vapor absorption in the region near the OH transition of interest, but still apply tunable diode laser WMS for the primary industrial OH sensor.

The dual-comb spectrometer employed here consists of two linear-cavity, Er-doped fiber frequency comb lasers with a 200-MHz pulse repetition rate. Each comb is individually amplified using erbium-doped fiber amplifiers and then spectrally broadened with a section of highly non-linear fiber (HNLF). In the optical frequency domain, each comb

Fig. 3 Overview of the routine used to fit the measured WMS $2f/1f$ signal of the overlapping OH and H_2O features in order to extract OH mole fraction



produces hundreds of thousands of modes, which appear as narrow linewidth “comb teeth”, spaced by the pulse repetition rate of the laser. The broadened spectrum is then spatially filtered to the wavelength range of interest using a grating-based filter. This filtered light then passes through the gas sample of interest to probe the absorption in the NIR and infer the thermodynamic properties.

Once the light from both lasers passes through the gas sample, they interfere on a single photodetector. In order to read the signals from each comb tooth, the two combs are stabilized to slightly different pulse repetition

rates, which results in a different frequency spacing of the comb teeth for each laser. Therefore, when the lasers are combined, the frequency difference between corresponding “comb teeth” results in a unique RF heterodyne frequency at an integer multiple of the difference between repetition rates, Δf_{rep} . The resulting time-domain signal on the detector is a series of interferograms which repeat at the difference frequency between the two comb repetition rates. A Fourier transform of these interferograms reveals the transmission spectrum including attenuation due to absorption from the measured gas. Further description of

the specific DCS method and spectrometer applied here can be found in Refs. [52–54].

3 High-temperature H₂O absorption database development using dual-comb spectroscopy in a premixed flame

We utilize dual-frequency comb spectroscopy (DCS) measurements in a well-characterized flame to develop a high-temperature H₂O absorption database near 1.5 μm . The absorption line parameters are extracted from DCS data using the multispectral fitting code described in Refs [30, 31]. This section will provide an overview of the database extraction process, as highlighted in Fig. 4.

To extract a new database from measurements in the flame, we provide the multispectral fitting code with three inputs: (1) an estimated linelist to provide seed input values for the location, strength, and shape of transitions; (2) measured transmission data from the flame; and (3) the known thermodynamic properties (temperature, pressure, etc.) along the laser line-of-sight during the measurement. We utilize the H₂O line parameters from HITEMP 2010 for the seed absorption database [25]. DCS measurements near 1491 nm at three different flame conditions provide the input transmission data. Fits of the DCS-measured transmission from a different wavelength region where a published high-temperature experimental database exists [29] provide the line of sight thermodynamic properties of the flame. The multispectral fitting routine uses the three inputs to fit all three data sets simultaneously to determine

the optimal set of absorption line parameters for the new database. We then compare a simulation created using the new high-temperature H₂O database to measured DCS data at a fourth premixed flame condition to test the new parameters.

3.1 Transmission measurements

The multispectral fitting routine is able to generate the best possible list of spectral absorption parameters if it is provided measurements at different temperatures, pressures, and species mole fractions. Many of the H₂O transitions measured in combustion conditions near 1491 nm are not detectable (without cavity enhancement) except at high temperatures; thus, we require a gas sample above 1700 K containing sufficient H₂O to generate detectable absorption for stable fits. By probing a premixed flame, we can achieve high temperatures in a uniform manner. The burner system used in this work for extraction of line parameters is a ribbon burner, which is a burner consisting of a series of small flame jets [55]. These burners have been shown to produce stable flames that result in uniform temperature fields that can be used for industrial processing [56]. Since the ribbon burner is a premixed flame, OH will be produced in the reacting zone of the flame and then decrease toward equilibrium values for the temperatures present above the flame. We present a characterization of the OH within and above the reacting zone of the ribbon burner in Sect. 4.1 to demonstrate that the WMS sensor indeed measures OH instead of additional H₂O absorption.

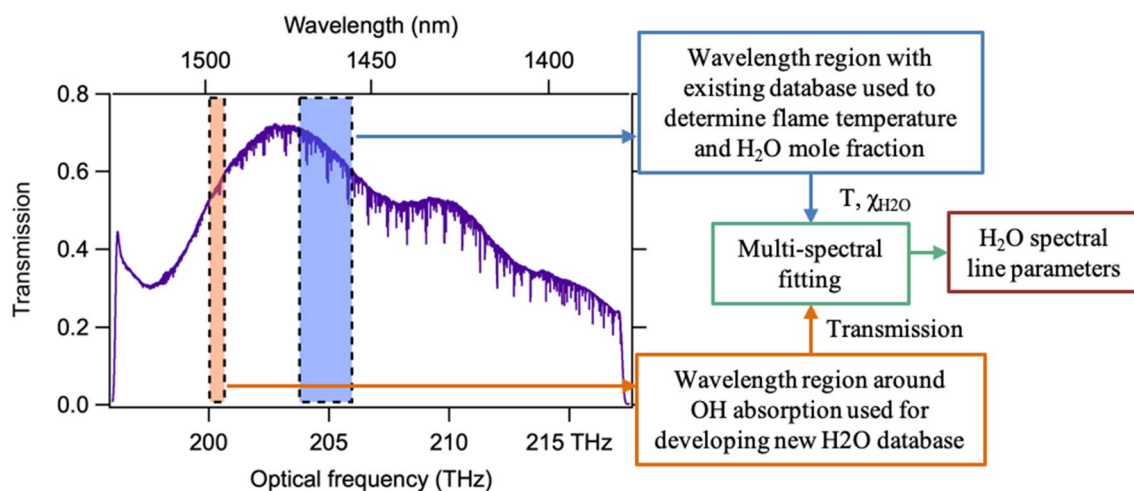


Fig. 4 Flow chart of high-temperature, H₂O absorption experimental linelist development. The purple trace is the transmission measured by dual-frequency comb spectroscopy above a premixed flame operating at 90 W/cm² and $\phi=0.9$. Shading highlights wavelength regions used to provide the transmission data for the linelist (orange) and temperature and H₂O mole fraction (blue) inputs to multispectral

fitting routine. The orange region contains the OH absorption transition used for the industrial WMS sensor. H₂O transitions in the blue region have previously been validated by Schroeder et al. [27]. The multispectral fitting routine uses these two inputs from several spectra to extract a new list of H₂O spectral line parameters

Table 1 Premixed ribbon burner conditions for the four measurements used for spectral line parameter measurements

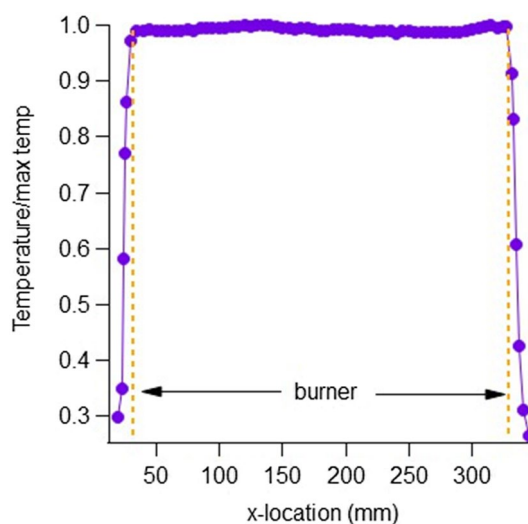
Condition #	Fuel (SLPM)	Air (SLPM)	Equivalence ratio	Power flux (W/cm ²)
1	6.28	76.1	0.8	79
2	7.00	75.3	0.9	88
3	7.36	75.3	0.95	93
4	7.70	74.6	1	97

The ribbon burner combusts premixed methane and air at controlled conditions, as described in Ref. [45]. Low-power fluxes, approximately 90 W/cm², were selected to keep the visible flame short and gas velocity low. By keeping the flame short, the laser can probe the product gases above the visible flame at a distance close to the burner surface, which helps to minimize non-uniformity across the flame due to buoyancy-driven necking and entrainment of surrounding air (which occurs at larger heights above the burner). Air and fuel flow rates were adjusted to achieve varying fuel–air equivalence ratios while maintaining a consistent flame height. The laser light from the frequency combs passes along the length of the burner at approximately 7 mm above the surface, as shown in Fig. 2.

The flame conditions and reactant flow rates for the four measurement conditions are given in Table 1. Data using the dual comb spectrometer are collected at each of the four conditions for 30 min and a background data set is collected for 20 min while the air is flowing at 100 SLPM. A sample of the transmission spectrum is shown in Fig. 4, with the gold region highlighting the wavelength range of interest for OH detection. The 30-min averaged transmission data for three out of the four conditions are used with the background data as an input for the multispectral fitting. Condition #3 is retained as a test case to validate the spectral parameters measured from the other three cases.

3.2 Line-of-sight thermodynamic properties of the premixed flame

In order to minimize uncertainty in the extracted line parameters, it is important to create a known, spatially uniform thermodynamic profile along the laser beam. We characterize the spatial uniformity of the ribbon burner test bed by probing the temperature profile along the beam path with a type-K thermocouple. The thermocouple bead is 1.65 mm, approximately the size of the laser beam diameter. The thermocouple is placed in the beam path on a horizontal translation stage, as shown in Fig. 2. Figure 5 shows the thermocouple-measured temperature normalized by the maximum temperature. There is 1.4% maximum variation measured between the bounds of the burner (denoted by

**Fig. 5** Normalized temperature measured with a type-K thermocouple in the beam path

gold-dash lines) and a steep gradient on each side. Similar uniformity is achieved for all four trials. The 297-mm width of the uniform region is taken to be the pathlength for the multispectral fitting.

The thermocouple characterizes the uniformity along the beam path, but does not accurately measure the absolute temperature due to radiative, convective, and conductive losses around the thermocouple tip. Instead, we utilize the dual-comb spectrometer measurements from 1455.3 to 1469.5 nm (204–206 THz) where a high-temperature database has already been created using a tube furnace [29] to calculate the thermodynamic properties for each condition. The measured transmission within this wavelength range (highlighted in the blue box in Fig. 4) is fit with a model to extract the temperature, H₂O, and OH mole fractions. The fitting routine (described in Ref. [57]) uses line parameters provided by Schroeder et al. [29] for H₂O and HITEMP 2010 [25] for OH. The resulting measured thermodynamic properties for all four trials are shown in Table 2. The equilibrium H₂O and OH mole fractions are calculated using NASA CEA [58] at the measured temperatures. The measured OH mole fraction is on average 20% higher than the equilibrium calculations. This trend is consistent with the expectation that OH concentrations will decrease toward the equilibrium value as the reaction comes to completion above the visible region of the flame.

3.3 High-temperature absorption linelist

We now use three of the four measured conditions to create the experimental linelist, leaving the data condition #3 to test the experimental linelist. To begin, we evaluate the line-strengths at both 296 K and 2200 K for the 83,000 lines in

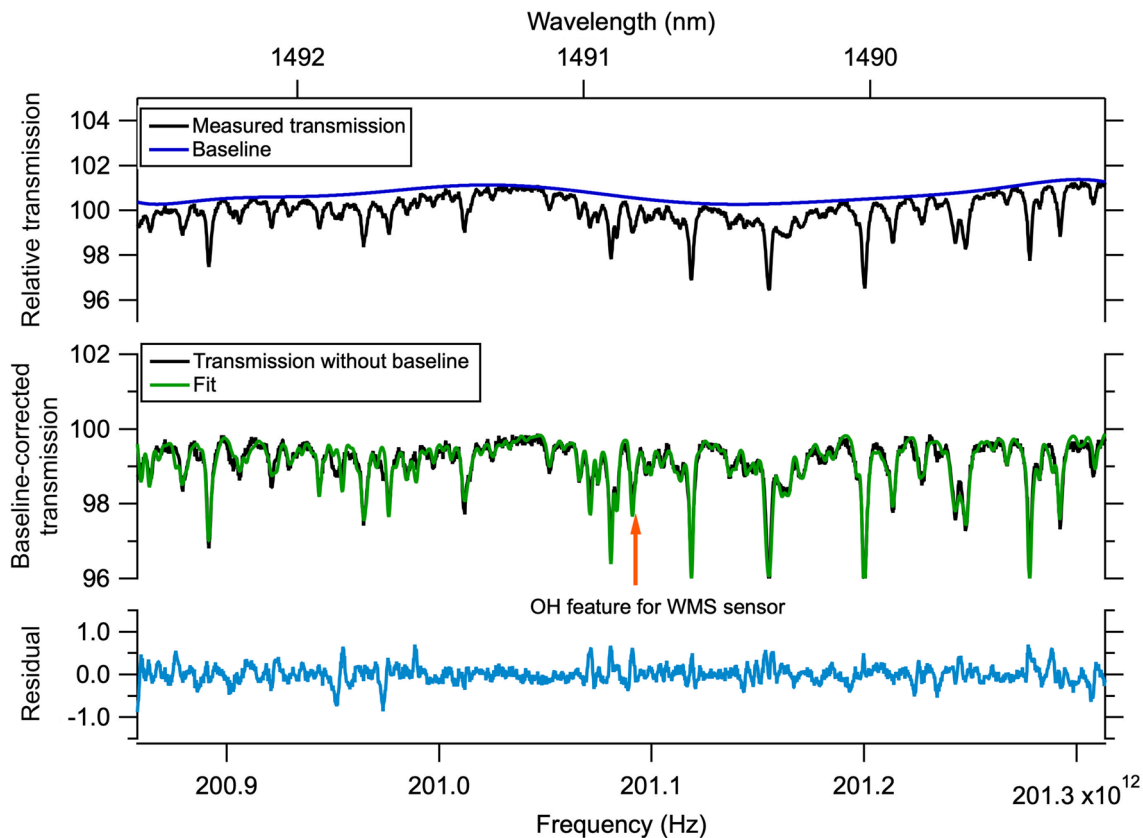
Table 2 Flame conditions measured by DCS and used for the multispectral fitting routine to extract H₂O absorption transition parameters near 1491 nm

Condition #	Equivalence ratio	Measured temperature (K)	Adiabatic temperature (K)	Measured H ₂ O mole fraction	Equilibrium H ₂ O mole fraction	Measured OH mole fraction	Equilibrium OH mole fraction
1	0.8	2019	1994	0.162	0.153	0.00275	0.00212
2	0.9	2119	2130	0.181	0.169	0.00354	0.00316
3	0.95	2154	2184	0.187	0.177	0.00389	0.00341
4	1	2165	2220	0.191	0.184	0.00385	0.00316

the 1489–1492.5 nm (200.8–201.4 THz) spectral region of the HITEMP database, and apply a 3×10^{-26} cm⁻¹/atm line-strength filter. The threshold reduces the database to 1983 H₂O lines and 4 OH lines. These lines produce absorption features above the noise floor at the measured conditions. The multispectral fitting routine uses the line parameters from the seed list as initial guess values to simulate absorbance as a function of wavelength as a series of Voigt profiles. This simulated line-by-line absorbance from H₂O and OH is combined with a 9th order Chebyshev polynomial baseline to produce a transmission model that is compared to the measured transmission for a given condition. Residuals

between this model and the measured transmission spectra are calculated for each condition.

The multispectral program iteratively fits the Chebyshev baseline and H₂O spectral parameters to the measured transmission spectra. OH parameters are not varied because it is difficult to achieve controlled quantities of OH and the database parameters are typically assumed to be sufficient, such as in Ref [22]. The linecenters are scaled to burner conditions using the HITEMP air-shift parameter with a temperature-dependence exponent of unity [50]. The self-shift was fixed to zero because HITEMP does not provide ab initio coefficients and Schroeder et al. [29] was not able

**Fig. 6** (Top) Relative transmission measured during trial 2 with baseline fit from multispectral analysis. (Middle) Baseline-corrected transmission (black), multispectral fit result (green), and fit residual (blue)

to observe the H₂O self-shift in a multispectral fit to a neighboring spectral region. An example of this fitting is shown in the top panel of Fig. 6, which shows the measured relative transmission for condition #2 and the Chebyshev baseline. First, the Chebyshev polynomial coefficients are fit to each transmission spectrum using the seed database absorption model. Then, the reference linestrengths S_{296} are floated to minimize fit residuals. If the floated linestrength of a particular transition is not stable within the reported statistical uncertainty of the multispectral fit after ten iterations, the linestrength is fixed back to its HITEMP value. Of the 1983 HITEMP transitions above the measurement threshold in this spectral region, 82 were found to produce stable linestrength fits that reduced the multispectral fit residual. All others were fixed at the HITEMP value because the signal-to-noise ratio and range of thermodynamic conditions were insufficient to produce stable fits. Next, self-broadening coefficients are systematically floated in the multispectral fit. Self-broadening was chosen over foreign broadening as the measured gases are 18–20% H₂O and H₂O induces significant self-broadening. Of the 82 transitions with floated

linestrength, only 14 produced stable self-broadening fits that reduced the fit residual. Finally, a single linecenter was floated for a strong transition that showed clear evidence of an incorrect linecenter. The spectral parameters of the 28 H₂O doublets in the spectral range are constrained to each other according to the procedure in [29, 51]. The baseline-corrected transmission spectra for condition #2, normalized to 100, is shown in black in the middle panel of Fig. 6 with a simulation of the final linelist and the corresponding residuals on the bottom panel.

Having extracted absorption line parameters for H₂O in the 1489–1492.5 nm (200.8–201.3 THz) region, we test the new experimental linelist using the measured spectrum of condition #3 ($\phi = 0.95$, 93 W/cm²). The measured absorbance is shown in black in Fig. 7. We compare the measured absorbance to simulated absorbance created from HITEMP 2010 (green) and the experimental line list (pink). Each simulation is compared to the measured data to produce the residuals shown in the top axis of Fig. 7. It is clear from Fig. 7 that the residuals for the simulation using the experimental linelist are smaller across almost all frequencies, suggesting the experimental linelist

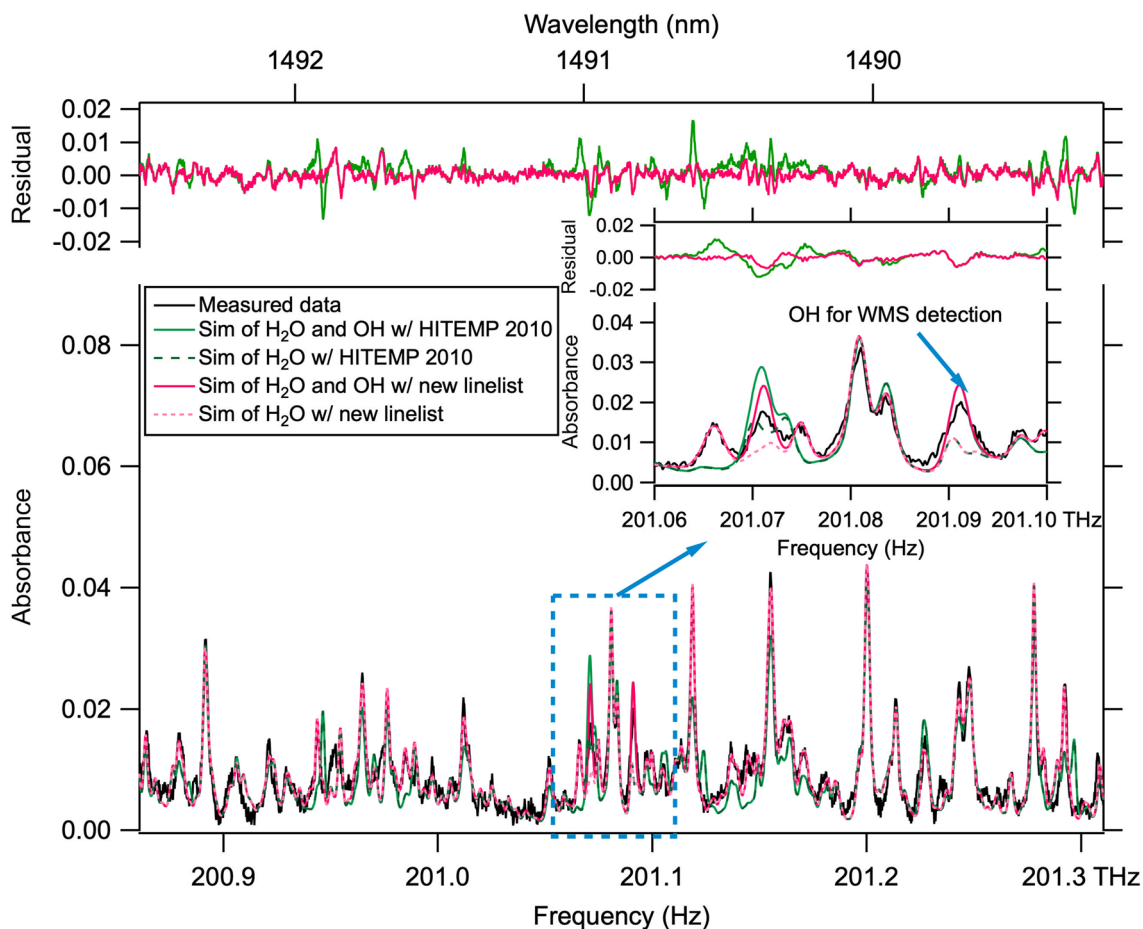


Fig. 7 Measured absorbance as a function of optical frequency as compared to absorbance simulated with HITEMP 2010 (green) and the experimental database (pink) at the measured thermodynamic properties. The resulting residuals between model and fit are shown as the top traces

improves on HITEMP 2010 under these conditions. The inset of Fig. 7 illustrates the improved agreement near the OH transition that will be used by the WMS sensor. For linestrength, 36 of the new linestrengths deviate less than 50% and 65 deviated less than 200% from HITEMP 2010.

Uncertainties of the extracted line parameters in the new linelist fall into two categories: transition-specific and transition-independent. The transition-independent uncertainties are based on the systematic uncertainties of the experiment and will be the same for all extracted parameters. By simplifying the equation for temperature-dependent linestrength:

$$S(T) = S_0 \frac{Q(T_0)}{Q(T)} \left(\frac{T_0}{T} \right) \exp \left(-\frac{hcE''}{k} \left(\frac{1}{T} - \frac{1}{T_0} \right) \right) \times \left(1 - \exp \left(\frac{-hc\nu_0}{kT} \right) \right) \left(1 - \exp \left(\frac{-hc\nu_0}{kT_0} \right) \right)^{-1} \quad (3)$$

where T is the temperature of interest, S_0 or $S_{296\text{K}}$ is the strength of the absorption transition at the reference temperature T_0 (296 K), $Q(T)$ is the partition function at a given temperature, E'' is the lower state energy state of a transition, ν_0 is the center frequency of the transition, and hc and k are Planck's constant and the Boltzmann constant, respectively. Because ν_0 will be approximately the same for all transitions measured in this work we can simplify this expression to:

$$S(T) = S_{296\text{K}} \beta(T) \quad (4)$$

where $\beta(T)$ contains the temperature dependence of the linestrength, simplified to:

$$\beta(T) = \left(\frac{296}{T} \right)^{2.77} \exp \left(-\frac{1.435E''}{T} \right) \quad (5)$$

We can then solve Eq. (2) for $S_{296\text{K}}$ to give:

$$S_{296\text{K}} = \frac{A}{\beta(T)PXL} \quad (6)$$

The uncertainty on each of the independent variables on the right-hand side of Eq. (6) contributes to the overall systematic linestrength uncertainty. Temperature and mole fraction uncertainties from the fit to the 1455.3–1469.5 nm (204–206 THz) spectral region propagate to $S_{296\text{K}}$ uncertainties according to Eqs. (5) and (6). In particular, temperature uncertainty will propagate as an uncertainty of $\beta(T)$. Pressure and path length uncertainty are captured in the uncertainty of the mole fraction fit, and thus a single value of uncertainty for the product of PXL is reported based on the mole fraction fit uncertainty. The integrated area (A) uncertainty is attributed to any nonlinearity in DCS measurements.

We can, therefore, estimate the transition-independent uncertainty of the extracted reference linestrength to be the sum of the uncertainties of each of these quantities in quadrature,

$$\frac{\delta S_{296\text{K}}}{S_{296\text{K}}} = \sqrt{\left(\frac{\delta A}{A} \right)^2 + \left(\frac{\delta \beta}{\beta} \right)^2 + \left(\frac{\delta PXL}{PXL} \right)^2} \quad (7)$$

which is approximately 7%. This analysis assumes 0.5% uncertainty in A based on a conservative estimate of the frequency comb linearity in these experiments [59], 5.5% uncertainty in β from temperature uncertainty, and an average E'' and 3.8% uncertainty in PXL from the uncertainty in DCS fitting for X .

We estimate the transition-specific uncertainty as a product of statistical uncertainty of the multispectral fitting routine and the stability of the fit. The statistical uncertainty for each fit parameter is extracted with the new line parameter and is tabulated in the Appendix A of ESM. We determined the fit stability by perturbing the stable $S_{296\text{K}}$ and self-broadening values by a normal distribution of uncertainties with a standard deviation of 10% and iterating the multispectral fitting with these new parameters. Select parameters were unstable in this perturbation study due to the narrow range of conditions covered in the data. This perturbation uncertainty is also tabulated with the new linelist parameters in the Appendix A of ESM. These transition-specific linestrength uncertainties should be included together with the transition-independent linestrength uncertainty (7%) to determine the overall linestrength uncertainty for any particular transition.

It is important to note that the linestrength and self-broadening values measured in this work are primarily for use under similar temperature and pressure conditions as those demonstrated here. Because of the small temperature and pressure range over which these parameters were obtained, it is not suggested that these parameters be extrapolated over large ranges, as one might do with lists obtained from data over larger ranges.

4 Demonstration of WMS OH radical sensor

While the broadband, high-resolution nature of DCS provides greater accuracy and flexibility, WMS is a robust, high time-resolution, lower-cost option for a targeted measurement of a particular species. As described in Sect. 2.2, OH and H_2O significantly overlap and interfere with one another in the near-infrared spectral region. Therefore, the OH mole fraction must be extracted from measured WMS signals which include absorption by both H_2O and OH. We use the measured high-temperature H_2O linelist as the basis for data analysis in the WMS sensor. The new WMS sensor is used to characterize OH in both a premixed flame system known to contain OH, and a catalytic combustor system with unknown OH content.

4.1 OH measurements in a premixed flame

We first demonstrate our WMS sensor in a system that is known to produce OH. The premixed ribbon burner described in Sect. 3.1 and used to produce the H₂O linelist, was shown via modeling by Sullivan et al. [60] to have OH mole fractions up to 7×10^{-3} . We use higher methane and air flow rates than those used to produce absorption spectra for the linelist retrieval (equivalence ratio of 0.95 and power flux of approximately 500 W/cm²). This results in visible flames that are several centimeters tall. Measurements are made across the flame at 2-mm vertical intervals for the first 1 cm and 5-mm vertical intervals up to 5 cm. Each measurement is averaged for 30–60 s to account for turbulent fluctuations in the flame.

Figure 8a–c shows the measured $2f/1f$ signals at three of the heights above the burner surface to illustrate how

the H₂O and OH absorption signals change in the premixed flame. The signals at 1392 nm and 1469 nm, shown in Fig. 8a, b, represent H₂O absorption with two different lower state energies (E''), which give the features different temperature dependencies. The consistent magnitude of the signals in both (a) and (b) at all three heights suggests that H₂O and temperature are relatively constant at these three heights. On the other hand, the measured $2f/1f$ signal at 1491 nm in Fig. 8c drops by 50% between 7 and 38 mm, which follows the expected trend for OH. If the signal arose from H₂O absorption from any of a variety of lower state energy levels, we would not expect such a change. This is further highlighted in Fig. 8d, which shows the vertical profiles for temperature, H₂O and OH mole fraction in the premixed flame. Both temperature and H₂O increase initially and then become stable as the combustion process is complete. The green (triangle) trace in 8(d) shows that the

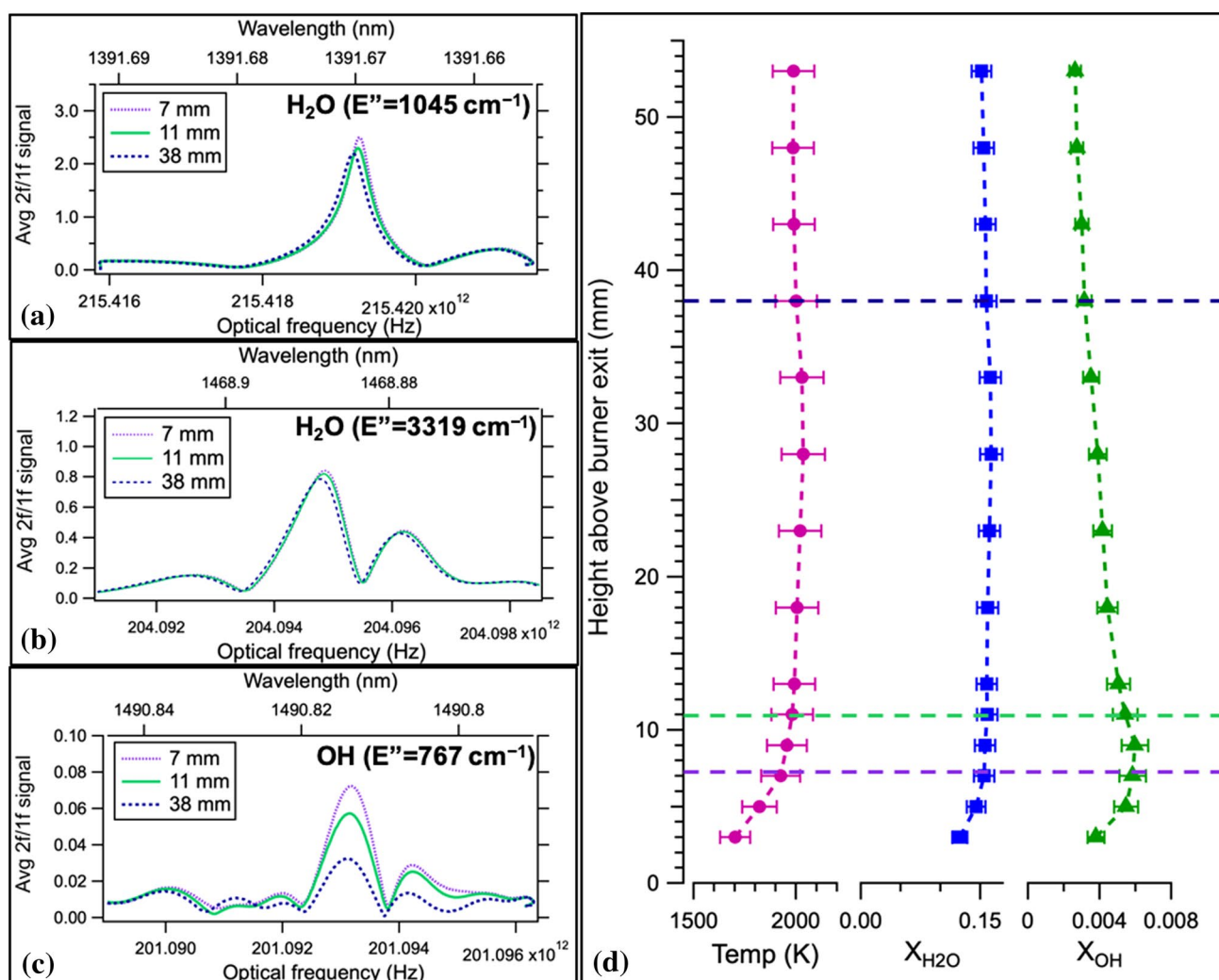


Fig. 8 Measured $2f/1f$ at three heights above burner exit using lasers at **a** 1391.7 nm to measure H₂O, **b** 1468.9 nm to measure H₂O and **c** 1490.8 nm to measure OH. **d** Measured average temperature, H₂O, and OH mole fractions as the beam is scanned vertically in the flame

measured OH mole fraction in the flame using the 1491 nm WMS measurements initially increases, followed by a rapid decline. We measure a peak mole fraction of OH of 0.006 with an uncertainty of 8×10^{-4} , which is very close to the maximum of approximately 0.007 predicted by the simulations in Ref. [60].

4.2 OH measurement in a catalytic combustor

In industry, catalytic combustors can be used to reduce emissions from processes requiring combustion, and as a nominally non-reacting heat source. Introducing a catalyst lowers the energy required for the dissociation of combustion reactants, with the goal of obtaining more complete combustion with lower emissions [61, 62]. Because the catalyst reduces combustion temperatures to 1400–1600 K, we do not expect to find equilibrium OH mole fraction levels above 10^{-4} if combustion is complete. Therefore, sensing OH at the exit of a catalytic combustor can provide insight into the effectiveness of the catalyst at achieving complete combustion, or the health of a catalyst in long-term monitoring applications.

We send the combined laser light of the WMS sensor in a triple pass arrangement across the surface of the combustor to probe the product gases exiting the combustor. Four combustor power fluxes were selected from 5 to 20 W/cm². At 5 W/cm² the catalytic bed is barely glowing, which suggests low temperatures that are not conducive to the existence of OH. On the other hand, when the burner operates at 20 W/cm² there is a visible blue flame at the surface of the catalytic bed that indicates a high likelihood of continued combustion and the possible presence of detectable OH concentrations. At each power flux the equivalence ratio is varied by fixing the methane flow rate and varying the air flow rate to change the combustion chemistry and conditions at

the surface. Thus, the $\phi = 0.6$ case corresponds to the highest air flow rate and, therefore, the highest exit velocity for a given power flux.

Figure 9a, b shows the measured temperature and H₂O mole fraction as a function of equivalence ratio for the four power flux conditions selected. Vertical uncertainty bars are 4% and 7%, respectively, which is the sensor uncertainty derived from validations under known conditions [47] and the uncertainty of experimental conditions. The increase in both properties with equivalence ratio matches expectations that each will reach a maximum near or slightly above the stoichiometric ($\phi = 1$) condition. Additionally, the traces in Fig. 9a confirm that higher temperatures occur at higher fuel flow rates.

The OH mole fraction trends are shown in Fig. 9c. Time-resolved OH mole fraction results indicate that the precision of the measurement is about 1.6×10^{-5} at 1700 K for the data presented here with a pathlength of 75 cm and 2.9×10^{-4} at 2000 K with a pathlength of 90 cm. The precision is used here as an estimate of the lowest detectable level of OH. The uncertainty of OH mole fraction values is approximately 9%, which is calculated by adding in quadrature the uncertainties of temperature, H₂O mole fraction, pressure, pathlength and $S(T)$ as per Eq. (2).

Combustion should be complete, and the equilibrium level of OH at the gas temperatures above the catalyst should be $\sim 10^{-4}$; thus, it is surprising to see indications of OH radical present above the catalytic combustor surface. For the lower power flux conditions, OH concentration decreases with equivalence ratio. This trend opposes both the expected trend of increasing equilibrium levels of OH with increasing temperature and increasing OH concentrations in premixed combustion as equivalence ratio increases [60]. In the case of the lowest power flux (5 W/cm²), the OH mole fraction

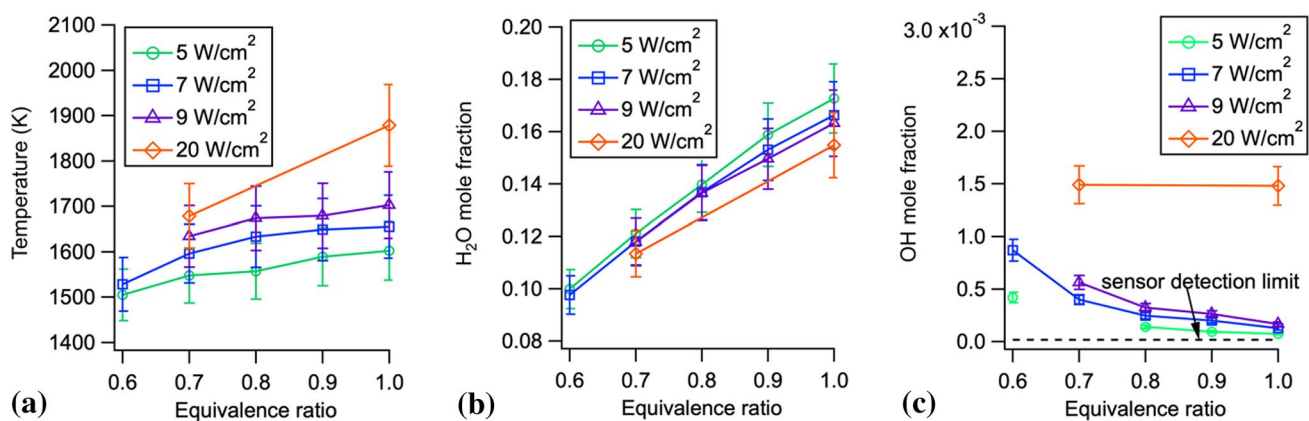


Fig. 9 **a** Temperature, **b** H₂O mole fraction and **c** OH mole fraction as a function of equivalence ratio for a range of power fluxes measured at the surface of a catalytic combustor using WMS. Uncertainty bars for **a** and **b** are 4% and 7%, respectively, from measurements in

a fixed-temperature furnace in Ref. [36]. The uncertainty bars for **c** are 9%, which are estimated from the combined H₂O and temperature measurement uncertainties and uncertainty in $S_{296\text{ K}}$ values extracted in this work

measured at $\phi = 0.6$ is significantly larger than the other conditions (where OH levels are very close to the detection limit of the sensor). The OH, therefore, appears to trend with air flow rate, instead of temperature or equivalence ratio, indicating that the catalyst may not have sufficient residence time or high enough temperatures in the catalyst-bed to react all of the fuel and oxidizer at higher flow rate cases. Whether this trend is due to a saturation of the available active sites on the catalyst or residence time issues is not clear, but this condition is not ideal for certain industrial applications where reactive radicals in the product gases of the catalytic combustor are not desired. Overall, these measurements demonstrate the utility of the WMS OH sensor for studying the effectiveness of the catalyst under different conditions or for long-term industrial monitoring of catalyst health.

5 Conclusion

In this work, we employ both wavelength modulation spectroscopy and dual-comb spectroscopy to develop an accurate and sensitive OH radical sensor near 1491 nm. The first dual-comb spectroscopy measurements above a controlled premixed flame are performed in order to develop a high-temperature absorption model for H₂O near 1491 nm. The air and fuel flow rates of a premixed ribbon burner are adjusted to achieve four different flame conditions for use in multispectral fitting to extract an empirical absorption linelist valid for similar combustion temperatures. Simulations of absorbance using the new experimental linelist are in better agreement with measured absorbance data at our flame conditions, as compared to simulations derived from HITEMP 2010.

The new experimental linelist is incorporated as part of an industrial OH sensor using wavelength modulation spectroscopy at 1491 nm, in order to properly account for unavoidable H₂O interference. The linelist serves as the basis for simulating absorbance as a function of wavelength for H₂O from 1489 to 1493 nm so that H₂O is accounted for when measuring the OH contribution of the WMS signal. Using this linelist results in a significant increase in measured OH, matching well with previous work done in premixed flames. Our sensor has an OH mole fraction detection limit of 1.6×10^{-5} at 1700 K with 75 cm pathlength.

We apply the sensor for characterization of a premixed flame from a ribbon burner and the gases above a catalytic combustor. Measurements of OH at 1491 nm in the premixed flame match the expected trend for OH. Probing the gases at the exit of the catalytic combustor at a variety of power flux and equivalence ratio conditions indicate the existence of additional combustion above the surface of the catalytic bed at high velocity and/or higher fuel flow rate conditions. The combined sensitivity of WMS, together with the accuracy

provided by the high-temperature spectral empirical linelist derived from DCS, make the sensor ideal for application to catalytic combustion, plasmas or premixed flame processes in industry. The time-resolved and accurate nature of the sensor is also ideal for long-term monitoring and control.

Acknowledgements Research sponsored by 3M Company.

References

1. S.J. Pachuta, M. Strobel, J. Adhes. Sci. Technol. **21**, 795 (2007)
2. M. Strobel, M.C. Branch, M. Ulsh, R.S. Kapaun, S. Kirk, C.S. Lyons, J. Adhes. Sci. Technol. **10**, 515 (1996)
3. Z. Guoli, Z. Aimin, W. Jiating, L. Zhongwei, X. Yong, Plasma Sci. Technol. **12**, 166 (2010)
4. N. Srivastava, C. Wang, T.S. Dibble, Eur. Phys. J. D **54**, 77 (2009)
5. R. Grün, H.-J. Günther, Mater. Sci. Eng. A **140**, 435 (1991)
6. P. Bruggeman, D.C. Schram, Plasma Sources Sci. Technol. **19**, 045025 (2010)
7. J.W. Daily, Prog. Energy Combust. Sci. **23**, 133 (1997)
8. M.J. Dyer, D.R. Crosley, Opt. Lett. **7**, 382 (1982)
9. J.M. Seitzman, R.K. Hanson, P.A. DeBarber, C.F. Hess, Appl. Opt. **33**, 4000 (1994)
10. B.B. Dally, A.N. Karpetsis, R.S. Barlow, Proc. Combust. Inst. **29**, 1147 (2002)
11. J.R. Gord, T.R. Meyer, S. Roy, Annu. Rev. Anal. Chem. **1**, 663 (2008)
12. S. Kostka, S. Roy, P.J. Lakusta, T.R. Meyer, M.W. Renfro, J.R. Gord, R. Branam, Appl. Opt. **48**, 6332 (2009)
13. A.M. Steinberg, I. Boxx, C.M. Arndt, J.H. Frank, W. Meier, Proc. Combust. Inst. **33**, 1663 (2011)
14. R. P. Lucht, *Laser Spectroscopy and Its Applications*. (Taylor & Francis Group, 2017)
15. T. Fuyuto, H. Kronemayer, B. Lewerich, J. Bruebach, T. Fujikawa, K. Akihama, T. Dreier, C. Schulz, Exp. Fluids **49**, 783 (2010)
16. U. Azimov, N. Kawahara, E. Tomita, Fuel **98**, 164 (2012)
17. X. Cui, C. Lengignon, W. Tao, W. Zhao, G. Wysocki, E. Fertein, C. Coeur, A. Cassez, L. Croize, W. Chen, Y. Wang, W. Zhang, X. Gao, W. Liu, Y. Zhang, F. Dong, J. Quant. Spectrosc. Radiat. Transf. **113**, 1300 (2012)
18. G.J. Ray, T.N. Anderson, J.A. Caton, R.P. Lucht, T. Walther, Opt. Lett. **26**, 1870 (2001)
19. S. Wang, R.K. Hanson, Appl. Phys. B **124**, 37 (2018)
20. X. Mercier, E. Therssen, J.F. Pauwels, P. Desgroux, Chem. Phys. Lett. **299**, 75 (1999)
21. R. Peeters, G. Berden, G. Meijer, Appl. Phys. B **73**, 65 (2001)
22. L. Rutkowski, A.C. Johansson, D. Valiev, A. Khodabakhsh, A. Tkacz, F.M. Schmidt, A. Foltynowicz, Photonics Lett. Pol. **8**, 110 (2016)
23. T. Aizawa, Appl. Opt. **40**, 4894 (2001)
24. T. Aizawa, T. Kamimoto, T. Tamaru, Appl. Opt. **38**, 1733 (1999)
25. L.S. Rothman, I.E. Gordon, R.J. Barber, H. Dothe, R.R. Gamache, A. Goldman, V.I. Perevalov, S.A. Tashkun, J. Tennyson, J. Quant. Spectrosc. Radiat. Transf. **111**, 2139 (2010)
26. I.E. Gordon, L.S. Rothman, C. Hill, R.V. Kochanov, Y. Tan, P.F. Bernath, M. Birk, V. Boudon, A. Campargue, K.V. Chance, B.J. Drouin, J.-M. Flaud, R.R. Gamache, J.T. Hodges, D. Jacquemart, V.I. Perevalov, A. Perrin, K.P. Shine, M.-A.H. Smith, J. Tennyson, G.C. Toon, H. Tran, V.G. Tyuterev, A. Barbe, A.G. Császár, V.M. Devi, T. Furtenbacher, J.J. Harrison, J.-M. Hartmann, A. Jolly, T.J. Johnson, T. Karman, I. Kleiner, A.A. Kyuberis, J. Loos, O.M. Lyulin, S.T. Massie, S.N. Mikhailenko, N. Moazzen-Ahmadi,

- H.S.P. Müller, O.V. Naumenko, A.V. Nikitin, O.L. Polyansky, M. Rey, M. Rotger, S.W. Sharpe, K. Sung, E. Starikova, S.A. Tashkun, J.V. Auwera, G. Wagner, J. Wilzewski, P. Wcisło, S. Yu, E.J. Zak, *J. Quant. Spectrosc. Radiat. Transf.* **203**, 3 (2017)
27. P.J. Schroeder, D.J. Pfotenhauer, J. Yang, F.R. Giorgetta, W.C. Swann, I. Coddington, N.R. Newbury, G.B. Rieker, *J. Quant. Spectrosc. Radiat. Transf.* **203**, 194 (2017).
28. L. Rutkowski, A. Foltynowicz, F.M. Schmidt, A.C. Johansson, A. Khodabakhsh, A.A. Kyuberis, N.F. Zobov, O.L. Polyansky, S.N. Yurchenko, J. Tennyson, *J. Quant. Spectrosc. Radiat. Transf.* **205**, 213 (2018)
29. P.J. Schroeder, M.J. Cich, J. Yang, F.R. Giorgetta, W.C. Swann, I. Coddington, N.R. Newbury, B.J. Drouin, G.B. Rieker, *J. Quant. Spectrosc. Radiat. Transf.* **210**, 240 (2018)
30. D.C. Benner, C.P. Rinsland, V.M. Devi, M.A.H. Smith, D. Atkins, *J. Quant. Spectrosc. Radiat. Transf.* **53**, 705 (1995)
31. B.J. Drouin, D.C. Benner, L.R. Brown, M.J. Cich, T.J. Crawford, V.M. Devi, A. Guillaume, J.T. Hodges, E.J. Mlawer, D.J. Robichaud, F. Oyafuso, V.H. Payne, K. Sung, E.H. Wishnow, S. Yu, *J. Quant. Spectrosc. Radiat. Transf.* **186**, 118 (2017)
32. T. Fernholz, H. Teichert, V. Ebert, *Appl. Phys. B* **75**, 229 (2002)
33. R. Engelbrecht, *Spectrochim. Acta A Mol. Biomol. Spectrosc.* **60**, 3291 (2004)
34. K. Duffin, A.J. McGettrick, W. Johnstone, G. Stewart, D.G. Moodie, *J. Light. Technol.* **25**, 3114 (2007)
35. T. Cai, T. Tan, G. Wang, W. Chen, X. Gao, *Opt. Appl.* **39**, 13 (2009)
36. G.B. Rieker, J.B. Jeffries, R.K. Hanson, *Appl. Opt.* **48**, 5546 (2009)
37. H. Yang, D. Greszik, T. Dreier, C. Schulz, *Appl. Phys. B* **99**, 385 (2010)
38. G. Gao, B. Chen, B. Hu, *Spectrosc. Lett.* **47**, 6 (2014)
39. C.S. Goldenstein, C.A. Almodóvar, J.B. Jeffries, R.K. Hanson, C.M. Brophy, *Meas. Sci. Technol.* **25**, 105104 (2014)
40. L.J. Lan, Y.J. Ding, Z.M. Peng, Y.J. Du, Y.F. Liu, *Appl. Phys. B* **117**, 1211 (2014)
41. R. Sur, K. Sun, J.B. Jeffries, R.K. Hanson, *Appl. Phys. B* **115**, 9 (2014)
42. Z. Qu, R. Ghorbani, D. Valiev, F.M. Schmidt, *Opt. Express* **23**, 16492 (2015)
43. A. Behera, A. Wang, *Appl. Opt.* **55**, 4446 (2016)
44. Z. Wang, S.T. Sanders, M.A. Robinson, *Appl. Phys. B* **122**, 176 (2016)
45. T.R.S. Hayden, D.J. Petrykowski, A. Sanchez, S.P. Nigam, C. Lapointe, J.D. Christopher, N.T. Wimer, A. Upadhye, M. Strobel, P.E. Hamlington, G.B. Rieker, *Proc. Combust. Inst.* (2018). <https://doi.org/10.1016/j.proci.2018.05.058>
46. N. Polydorides, A. Tsekenis, E. Fisher, A. Chighine, H. McCann, L. Dimiccoli, P. Wright, M. Lengden, T. Benoy, D. Wilson, G. Humphries, W. Johnstone, *Appl. Opt.* **57**, B1 (2018)
47. T.R.S. Hayden, N.T. Wimer, C. Lapointe, J.D. Christopher, S.P. Nigam, A. Upadhye, M. Strobel, P.E. Hamlington, G.B. Rieker, *Combust. Sci. Technol.* **1**, 1 (2019)
48. R.K. Hanson, P.K. Falcone, *Appl. Opt.* **17**, 2477 (1978)
49. I. Coddington, N. Newbury, W. Swann, *Optica* **3**, 414 (2016)
50. P.J. Schroeder, M.J. Cich, J. Yang, W.C. Swann, I. Coddington, N.R. Newbury, B.J. Drouin, G.B. Rieker, *Phys. Rev. A* **96**, 022514 (2017)
51. J. Yang, P.J. Schroeder, M.J. Cich, F.R. Giorgetta, W.C. Swann, I. Coddington, N.R. Newbury, B.J. Drouin, G.B. Rieker, *J. Quant. Spectrosc. Radiat. Transf.* **217**, 189 (2018)
52. P.J. Schroeder, R.J. Wright, S. Coburn, B. Sodergren, K.C. Cossel, S. Droste, G.W. Truong, E. Baumann, F.R. Giorgetta, I. Coddington, N.R. Newbury, G.B. Rieker, *Proc. Combust. Inst.* **36**, 4565 (2017)
53. S. Coburn, C.B. Alden, R. Wright, K. Cossel, E. Baumann, G.-W. Truong, F. Giorgetta, C. Sweeney, N.R. Newbury, K. Prasad, I. Coddington, G.B. Rieker, *Optica* **5**, 320 (2018)
54. G.-W. Truong, E.M. Waxman, K.C. Cossel, E. Baumann, A. Klose, F.R. Giorgetta, W.C. Swann, N.R. Newbury, I. Coddington, *Opt. Express* **24**, 30495 (2016)
55. C.S. Alexander, M.C. Branch, M. Strobel, M. Ulsh, N. Sullivan, T. Vian, *Prog. Energy Combust. Sci.* **34**, 696 (2008)
56. M.C. Branch, N. Sullivan, M. Ulsh, M. Strobel, *Symp. Int. Combust.* **27**, 2807 (1998)
57. G.B. Rieker, F.R. Giorgetta, W.C. Swann, J. Kofler, A.M. Zolot, L.C. Sinclair, E. Baumann, C. Cromer, G. Petron, C. Sweeney, P.P. Tans, I. Coddington, N.R. Newbury, *Optica* **1**, 290 (2014)
58. S.M. Gordon, *Computer Program for Calculation of Complex Chemical Equilibrium Compositions, Rocket Performance, Incident and Reflected Shocks, and Chapman-Jouguet Detonations. Interim Revision, March 1976* (1976)
59. E.M. Waxman, K.C. Cossel, G.-W. Truong, F.R. Giorgetta, W.C. Swann, S. Coburn, R.J. Wright, G.B. Rieker, I. Coddington, N.R. Newbury, *Atmos. Meas. Tech.* **10**, 3295 (2017)
60. N. Sullivan, M.C. Branch, M. Strobel, J. Park, M. Ulsh, B. Leys, *Combust. Sci. Technol.* **158**, 115 (2000)
61. S.A. Cottillard, *Catalytic Combustion* (Nova Science Publishers Inc, Hauppauge, 2011)
62. R.E. Hayes, S.T. Kolaczowski, *Introduction to Catalytic Combustion* (CRC Press, Cambridge, 1998)

Publisher's Note Springer Nature remains neutral with regard to jurisdictional claims in published maps and institutional affiliations.